Surface and subsurface formation mechanism of SiC_p/Al composites under ultrasonic scratching

Qilin Li [a, b], Songmei Yuan [a, b,*], Xiaoxing Gao [a, b], Zikang Zhang [a, b], Bochuan Chen [a, b], Zhen Li [c], Andre D.L. Batako [d]

[a] School of Mechanical Engineering and Automation, Beihang University, Beijing, 100191, China
[b] Ningbo Institute of Technology, Beihang University, Ningbo, 315832, PR China
[c] Department of Mechanics and Aerospace Engineering, Southern University of Science and Technology, Shenzhen, 518055, China
[d] General Engineering Research Institute, Liverpool John Moores University, Liverpool, L3 5UX, UK

ABSTRACT

Rotary ultrasonic machining (RUM) is an effective method of high-quality and high-efficiency machining for advanced composites. However, the machining mechanism and kinematic characteristics of ultrasonic machining of SiC particles-reinforced aluminum matrix (SiC_p/Al) composites are yet unclear, limiting the applications of RUM in composites machining. In this study, a rotary ultrasonic vibration-assisted scratch (RUVAS) test was designed for the high-volume fraction of SiC_p/Al composites. The kinematic and scratch force model of RUVAS was developed to describe the scratch process of SiC_p/Al. Both RUVAS and conventional scratch (CS) tests were performed under various scratch speeds on SiC_p/Al. The scratch trajectory was divided into three modes: continuous, semi-continuous, and intermittent. We observed the formation of different surface morphology under different modes. The scratch force difference between RUVAS and CS was insignificant when the scratch speed is high, which indicated that the effect of ultrasonic vibration diminished at a high speed when the ultrasonic frequency was fixed. When assisted by ultrasonic vibration, the scratch morphology of SiC_p/Al indicated that the matrix has undergone significant plastic deformation. While the hard SiC particles tended to be ruptured and pressed into the plastic matrix, this mechanism can effectively suppress the initiation and propagation of cracks, which is beneficial to reducing the stress influence zone, healing the surface defects, and improving the surface integrity. The subsurface morphology indicates that the subsurface damage under CS and RUVAS mainly includes particle cracking, matrix tearing, and interface failure. Our experimental result shows that ultrasonic vibration can effectively reduce the subsurface damage of SiC_p/Al composites, bringing insight into fundamental mechanisms of ultrasonic machining and providing guidance for the vibration-assisted processing of SiC_p/Al composites.

1. Introduction

Metal Matrix Composites (MMCs) have earned themselves a wide range of applications in the industry with their excellent properties. Among the MMCs, silicon carbide particles-reinforced aluminum matrix composites (SiC_p/Al) have a low coefficient of thermal expansion, high wear resistance, stable thermal resistance, high specific strength, and excellent dimensional stability, which are considered ideal materials for aerospace structural and optical parts [1,2]. However, these excellent properties of SiC_p/Al also bring machining challenges due to the addition of abrasive and high-hardness SiC particles in the aluminum alloy matrix, which limits its extensive employment of SiC_p/Al. During conventional machining of SiC_p/Al, the cutting parameters were set to a lower threshold, cutting tools wear rapidly [3], and the machined surfaces have fractures, cracks, and micro pits with considerable sizes. The machining difficulties and defects in quality drive researchers to develop other machining technologies such as grinding, rotary ultrasonic machining(RUM), and high-speed machining(HSM) [4,5]. Compared with conventional grinding, rotary ultrasonic vibration-assisted machining has advantages in quality, efficiency, and cost in the processing of hard and brittle composites [6]. However, the material

---

* Corresponding author. School of Mechanical Engineering and Automation, Beihang University, Beijing, 100191, China.
E-mail addresses: liqilin93@buaa.edu.cn (Q. Li), yuansmbuaa@163.com (S. Yuan), gaoxiaoxing83@buaa.edu.cn (X. Gao), kdash@buaa.edu.cn (Z. Zhang), brucechen@buaa.edu.cn (B. Chen), liz33@sustech.edu.cn (Z. Li), a.d.batako@ljmu.ac.uk (A.D.L. Batako).

Nomenclature

RUVAS	rotary ultrasonic vibration-assisted scratch
CS	conventional scratch
n	spindle speed (rpm)
v_f	feed rate (mm · min^{-1})
v_s	linear cutting speed of diamond indenter (m · s^{-1})
r	distance between diamond tip and spindle center (mm)
A	maximum amplitude (μm)
f	frequency of ultrasonic vibration (Hz)
h_s	set depth of cut (μm)
h	practical scratch depth (μm)
C_l	length of lateral crack (mm)
C_h	depth of median crack (mm)
KIC	fracture toughness of SiCp/Al (MPa · m0.5)
E	Young's modulus of SiCp/Al (GPa)
β	half angle of the diamond tip (rad)
Fn	normal scratch force (N)
F_t	tangential scratch force (N)
μ	friction coefficient
λ	wavelength of diamond indenter's scratch motion (mm)
L_s	effective scratch distance on SiC$_p$/Al sample (mm)
Δt	time of scratch into and out of the sample surface (s)
σ	equivalent stress (MPa)
A	yield stress (MPa)
B	hardening modulus (MPa)
C	coefficient of strain rate sensitivity
m	coefficient of thermal softening
$n*$	coefficient of hardening
$\varepsilon^{\cdot}$	plastic strain
ε^n	strain rate
$\dot{\varepsilon}0$	reference plastic strain rate
T	temperature of material (K)
T_{melt}	melting temperature (K)
T_{room}	room temperature (K)
D	damage variable
$\Delta\varepsilon^{pl}$	increment of equivalent plastic strain
$\varepsilon pl\ f$	equivalent plastic strain when material failure
$\sigma*$	stress triaxiality
σ_t	maximum principal tensile stress (MPa)
U_n	crack normal displacement (mm)
$GI\ f$	fracture energy (N/m)
E'	equivalent Young's modulus of the SiC particle (MPa)
G	shear modulus of the SiC particle (MPa)
$eck\ nm$	strain of crack opening of the SiC particle

removal mechanism during rotary ultrasonic machining of SiC$_p$/Al is not yet clarified. Previous research studied the material removal mechanism of SiC$_p$/Al, but most of them either focused on SiC$_p$/Al with the low volume fraction of SiC (10%–25%) [7,8] or the material removal process was set at a low speed (1 mm· s^{-1}–100 mm·s^{-1}) [9–12]. These results are not reliable references to the actual rotary ultrasonic machining of SiC$_p$/Al with high volume fraction of SiC (45%–75%). To better understand the fundamental material removal mechanism of rotary ultrasonic machining of SiC$_p$/Al, it is important to explore the effect of scratch speed on the material behavior of SiC$_p$/Al with high volume fraction under ultrasonic vibration.

The machining difficulties of SiC$_p$/Al in conventional machining with carbide tool have proved itself an underperforming approach to SiC$_p$/Al processing, especially for SiC$_p$/Al with high volume fraction of particles. Huang et al. [13] used polycrystalline diamond(PCD) tools in high-speed milling of SiC$_p$/Al composites with higher volume fraction of SiC particles and found that even PCD tools wear quickly during the process. Liu et al. [14] found that the cutting force fluctuates significantly in the removal process because of reinforced particles. Yu et al. [7] investigated the relationship between tool position and particle failure behavior and found that the failure of particles is mainly caused by debonding, turning, and fragmentation.

Considering the low efficiency and high cost of conventional machining of hard and brittle composites, some researchers turn to adopting ultrasonic-assisted machining. Wang et al. [15] proved that rotary ultrasonic machining (RUM) with vertical ultrasonic vibration is an effective method to reduce the cutting force of hard and brittle composites. Bai et al. [16] conducted ultrasonic-assisted turning of SiC$_p$/Al with 25 vol% SiC particles reinforced. These experimental results showed a significant reduction in cutting forces with the assistance of ultrasonic vibration. Dong et al. [17] conducted both ultrasonic-assisted grinding and conventional grinding process on SiC$_p$/Al and found that the grinding force of ultrasonic-assisted grinding was 35–50% lower than that of conventional grinding. Zhou et al. [18] carried out the rotary ultrasonic face grinding of SiC$_p$/Al composites and the cutting force could be reduced by an average of 13.86%, and the surface roughness could be reduced by an average of 11.53% compared with conventional grinding. The vantage in the performance of ultrasonic-assisted machining led researchers to explore the fundamental mechanism involved in the ultrasonic-assisted machining process.

The scratch test with a single diamond grit is one of the most common methods to study material removal mechanisms. Kosel [19] identified the core difference between fixed-load and fixed-depth conditions for scratch tests and the use of fixed-depth scratch tests. These techniques are more suitable for those Class II materials—the dual-phase materials that contain large, hard second-phase particles such as carbides. Yin et al. [20] studied single diamond grain grinding of SiC$_p$/Al and found that the maximum stress was smooth during the removal process of the aluminum matrix but changed greatly whereas during the removal process of SiC particles. Wu et al. [21] investigated the depth of cut got a significant influence on the machined surface integrity. Their results indicated that the fracture of particles was mainly caused by high tensile stress from the shear deformation of the matrix and tool-particle interaction.

However, most conventional scratch test research did not address the effect of scratching speed, which is a major factor of practical machining. Li et al. [22] investigated single-abrasive scratch tests of C/SiC in two cutting directions under various cutting speeds. Liu et al. [23] conducted scratching experiments that covered the scratching speed from 10 mm .s^{-1} to 30 mm . s^{-1}. The results showed that tangential scratch force fluctuated slightly under a low range of scratching speed. Lin et al. [24] conducted a continuous scratch test on quartz glass with a speed of 6 m.min^{-1} to 15 m.min^{-1} and found that the area formed by high-speed cross-scratches is more damaged and entered brittle removal earlier than other areas. Yang et al. [25] studied the crack initiation mechanism by conducting scratch tests on BK7 glass with a speed of 1, 5, and 20 m.s^{-1}, which revealed the chipping critical depth becomes bigger when the speed is 5 m. s^{-1}. Meng et al. [26] studied the removal behavior of SiC with scratch speed from 10 m s^{-1} to 200 m s^{-1} and found that the hydrostatic stress of the processing region decreased as the scratch speed increased. It is obvious that scratch speed has an impact on material removal behaviors, which should be considered during scratch tests that can reflect practical machining situations under various cutting speeds.

To clarify material removal behaviors under ultrasonic-assisted machining, the researcher started to adopt ultrasonic-assisted scratch tests. Fujimoto et al. [27] took both an ultrasonic-assisted scratching test and a conventional scratching test on SiC ceramics. The results indicated that there are the intermittent mode and the continuous mode in the ultrasonic-assisted scratching process. Wang et al. [28] conducted scratching tests of carbon fiber-reinforced polymer (CFRP) composites and found that the material removal mode of CFRP could change from the ductile to the brittle fracture mode with the assistance of ultrasonic vibration. Feng et al. [9] conducted ultrasonic vibration-assisted scratch (UVAS) and traditional scratch tests of SiC_p/Al at low speed and it indicated that the average force of the UVAS processes was lower. Zheng et al. [10] conducted conventional scratch and ultrasonic vibration-assisted scratch tests of SiC_p/Al. and found that there is no brittle-ductile transition phenomenon for cutting depth in the scratch test of SiC_p/Al with a 45% volume fraction of SiC particles. However, previous studies have not mentioned the scratching speed, the surface, and subsurface formation during the ultrasonic vibration-assisted scratch test.

In our study, both rotary ultrasonic vibration-assisted scratch (RUVAS) test and conventional scratch test (CS) under various cutting speeds were studied on SiC_p/Al with a 65% volume fraction of SiC particles. The kinematic characteristics were analyzed and a scratch force model for RUVAS was developed to describe the scratch process. A finite element simulation model was established to explore the material removal process. The scratch trajectory characteristics and scratch force were compared between RUVAS and CS to illustrate the ultrasonic vibration effect on SiC_p/Al under various scratch speeds. The surface and subsurface morphology of samples were observed to reveal the surface integrity and subsurface damage of SiC_p/Al composites.

2. Kinematic characteristics of RUVAS

As shown in Fig. 1, the customized diamond indenter rotated at a speed of ***n*** with ultrasonic vibration in the Z-axis. The SiC_p/Al sample is fixed on an adjustable fixture which can change slope angle with an accuracy of 0.1° and moved at a speed of $\boldsymbol{v_f}$ in the positive direction of the X-axis.

The scratch trajectory is shown in Eq. (1):

$$\begin{cases} x = v_f \cdot t \\ y = v_S \cdot t = n \cdot 2\pi \cdot r \cdot t \end{cases} \tag{1}$$

where $\boldsymbol{v_s}$ denotes the linear speed of the diamond indenter, and ***r*** is the distance between the diamond tip and spindle center. During RUVAS the axial displacement ***z*** of the ultrasonic vibration is expressed as follows:

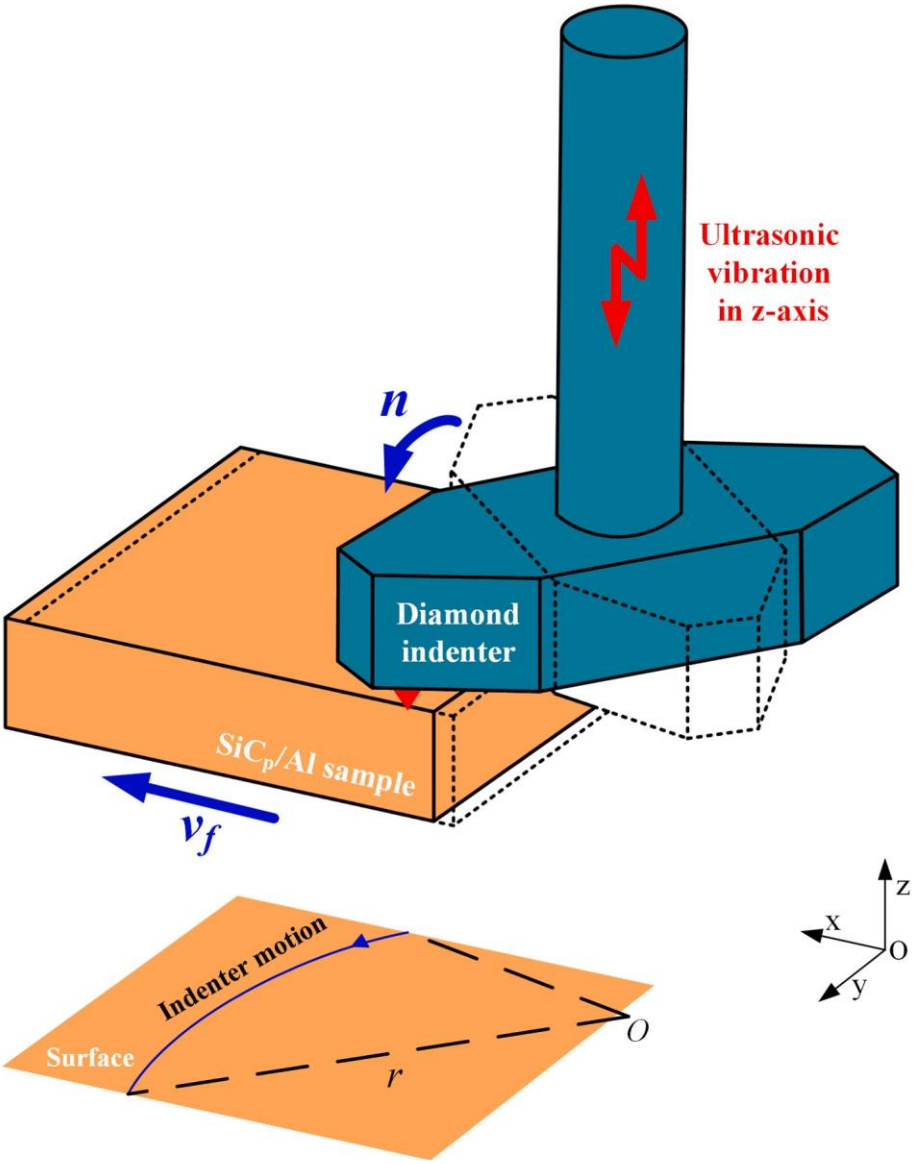

Fig. 1. Kinematic schematic diagram of RUVAS test.

$$z = A \sin 2\pi ft \tag{2}$$

where ***A***, ***f***, and ***h_s*** respectively denote the amplitude, the frequency of ultrasonic vibration, and the set depth of cut.

With these variables defined, the practical scratch depth ***h*** is derived as:

$$h = h_s + A \sin 2\pi ft \tag{3}$$

The scratch force of the SiC_p/Al composites is mainly composed of the plastic deformation force of the matrix, the brittle fracture force of SiC particles, and the friction force. Considering the high volume fraction of SiC particles in the samples discussed in this research, the SiC_p/Al composites are regarded as brittle materials. An interpretation of Marshall's ceramic crack theory in Fig. 2c shows the cracks induced by the diamond indenter. Here, the lateral crack has a length of $\boldsymbol{C_l}$ and the depth of median crack $\boldsymbol{C_h}$ can be expressed as

$$C_l = m\left[(E/H_V)^{3/4} \Big/ \left((a + b\ln(v_s/h_m))K_{IC}H_V^{1/4}\right)\right] F_n^{5/8} \tag{4}$$

$$C_h = C_2 \left(\frac{1}{\tan\beta}\right)^{1/3} \frac{E^{1/2}}{H_V} F_n^{1/2} \tag{5}$$

where ***m***, ***a***, ***b*** are constants related to the material-indenter subsystem; ***KIC*** is the fracture toughness of the sample; ***E*** is Young's modulus of the sample; ***vs*** is the cutting speed; ***β*** is the half angle of the diamond tip, ***Fn*** is the normal load applied to the diamond indenter; ***C2*** is a dimensionless constant, independent of the diamond indenter scratch system, ***C2*** = 0.226 [29].

The scratch force has two components, the tangential force $\boldsymbol{F_t}$ and the normal force $\boldsymbol{F_n}$. As a 136-degree diamond indenter scratched across the surface, the element of these force components are illustrated in Fig. 2b. According to Jahanmir's 'Mechanisms of Material Removal in Abrasive Machining of Ceramics' theory [30], the normal load F_n. can be calculated as given in Eq. (6):

$$F_n = k\left(\frac{K_{IC}^{1/2}H_V}{E^{2/5}}\right)\cdot\left(v_f/v_s\right)^{3/4} h^{1/4} \tag{6}$$

Substituting Eq. (3) into Eq. (6),

$$F_n = k\left(\frac{K_{IC}^{1/2}H_V}{E^{2/5}}\right)\cdot\left(v_f/v_s\right)^{3/4}(h_s + A\sin 2\pi ft)^{1/4} \tag{7}$$

where ***k*** is a constant relevant to the material.

Assuming that ***μ*** is the friction coefficient of SiC_p/Al, the tangential scratching force is written as:

$$F_t = \mu k\left(\frac{K_{IC}^{1/2}H_V}{E^{2/5}}\right)\cdot\left(v_f/v_s\right)^{3/4}(h_s + A\sin 2\pi ft)^{1/4} \tag{8}$$

Substituting Eq. (7) into Eq. (4), the lateral crack length $\boldsymbol{C_l}$ can be defined as follows:

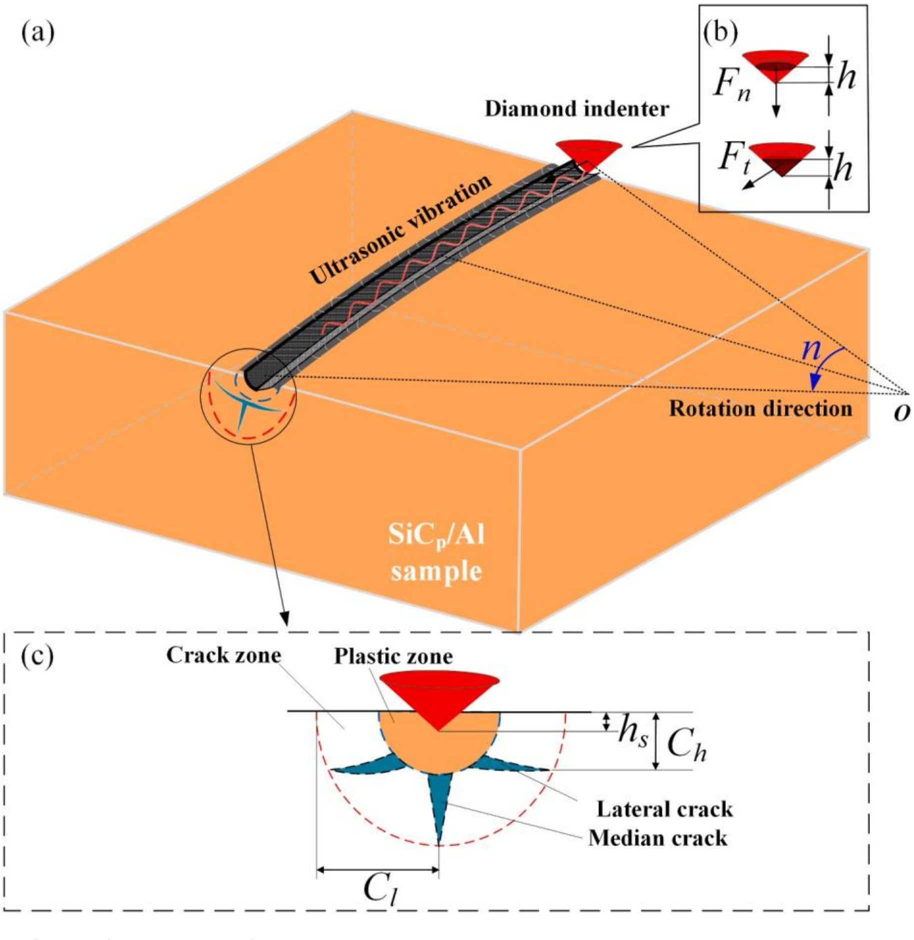

Fig. 2. Characteristics of material removal in RUVAS scratch test:
(a) an overview of the setting, (b) force components, (c) crack initiation.

$$C_l = \left[m\left(E/H_V\right)^{3/4}\Big/\left(\left(\left(a+b\ln(v_s/h_m)\right)K_{IC}\right)H_V^{1/4}\right)\right]\left[k\left(\frac{K_{IC}^{1/2}H_V}{E^{2/5}}\right)\cdot\left(v_f/v_s\right)^{3/4}\left(h_s+A\sin 2\pi ft\right)^{1/4}\right]^{5/8} \tag{9}$$

As the diamond indenter performs a sinusoidal motion due to the ultrasonic vibration, the cutting wavelength $\boldsymbol{\lambda}$ is expressed as Eq. (9):

$$\lambda = \frac{v_s}{f} = \frac{n\cdot 2\pi\cdot r}{f} \tag{10}$$

$\boldsymbol{L_s}$ is the effective scratch distance that the diamond indenter travels during the contact time $\boldsymbol{\Delta t}$ when the diamond tip scratch into and out of the sample surface. $\boldsymbol{L_s}$ and $\boldsymbol{\Delta t}$ can be expressed as follows:

$$L_s = n\cdot 2\pi\cdot r\cdot \Delta t \tag{11}$$

$$\Delta t \approx \frac{A+h_s}{2Af} \tag{12}$$

Substituting Eq. (12) into Eq. (11), $\boldsymbol{L_s}$ can be defined as follows:

$$L_s = n\cdot\pi r\cdot\frac{A+h_s}{Af} \tag{13}$$

When $0<\boldsymbol{h_s}\leq\boldsymbol{A}$, the ultrasonic vibration-assisted scratch motion turns to be intermittent as the diamond indenter moves inside and outside of the sample surface. Under this circumstance, the scratch trajectory appears to be continuous or intermittent depending on the relationship between $\boldsymbol{\lambda}$ and the length of the pit caused by scratch and maximum crack propagation. It indicates that the scratch trajectory is intermittent as mode I trajectory shown in Fig. 3 when $\boldsymbol{\lambda} > \boldsymbol{L_s} + \boldsymbol{C_{l\max}}$ which can also be expressed as

$$\frac{n\cdot 2\pi\cdot r}{f} > n\cdot\pi r\cdot\frac{A+h_s}{Af} + \left[m\left(E/H_V\right)^{3/4}\Big/\left(\left(\left(a+b\ln(v_s/h_m)\right)K_{IC}\right)H_V^{1/4}\right)\right]\left[k\left(\frac{K_{IC}^{1/2}H_V}{E^{2/5}}\right)\cdot\left(v_f/v_s\right)^{3/4}\left(h_s+A\right)^{1/4}\right]^{5/8} \tag{14}$$

When $\boldsymbol{\lambda} \leq \boldsymbol{L_s} + \boldsymbol{C_{l\max}}$, the scratch trajectory is continuous as the mode II or III trajectory which is shown in Fig. 3.

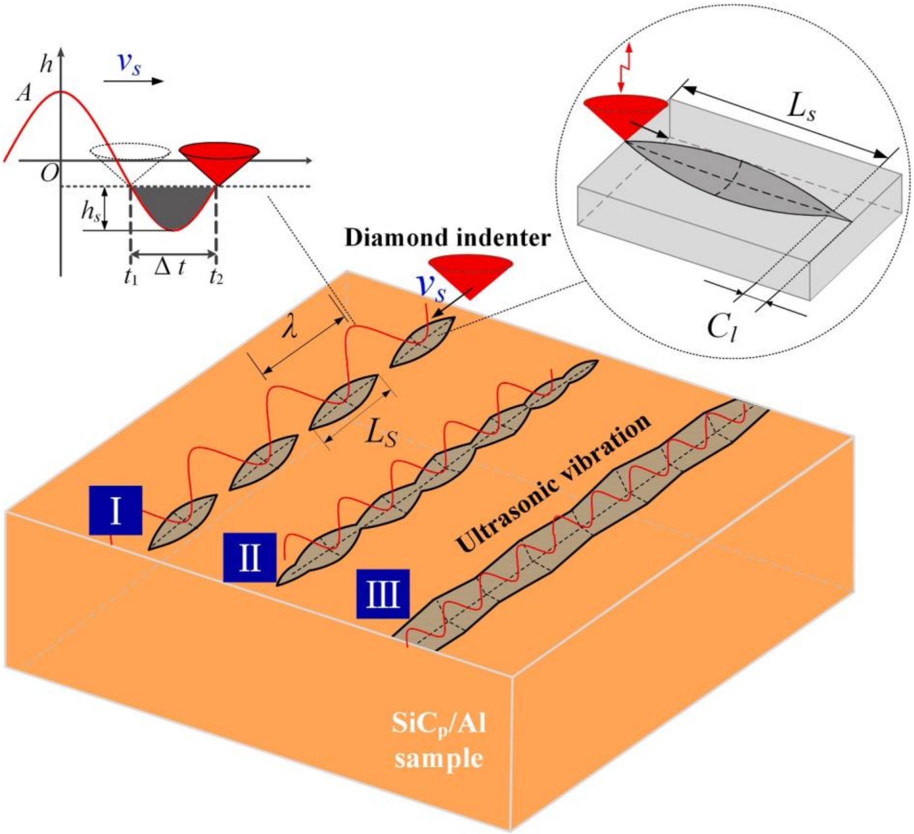

Fig. 3. Scratch trajectory mode of RUVAS.

3. Experiment and simulation

3.1. Experimental design

3.1.1. Sample preparation

The SiC$_p$/Al composites used in the investigation are manufactured by powder metallurgy. The properties of SiC$_p$/Al composites are listed in Table 1. The SiC$_p$/Al samples are divided into 10 mm*10 mm*5 mm sizes. To avoid interference of the original surface of SiC$_p$/Al with the scratch test, the surface is carefully lapped consecutively with diamond pastes of μm level grain sizes on an iron plate and polished to surface roughness Ra 0.1 μm. The polished surface is observed by SEM (JSM7500, JEOL Inc., Japan), as shown in Fig. 4.

Table 1

Properties of SiC$_p$/Al composites.

Properties	Value
Average size of SiC particles (μm)	80.0
Volume fraction of SiC (%)	65.0
Thermal conductivity (W. mK^{-1}, 373.15K)	73.0
Coefficient of thermal expansion (10^{-6}K^{-1})	12.0
Density (g $\cdot$ cm^{-3})	3.0
Elastic modulus (GPa)	188.0
Passion ratio	0.3

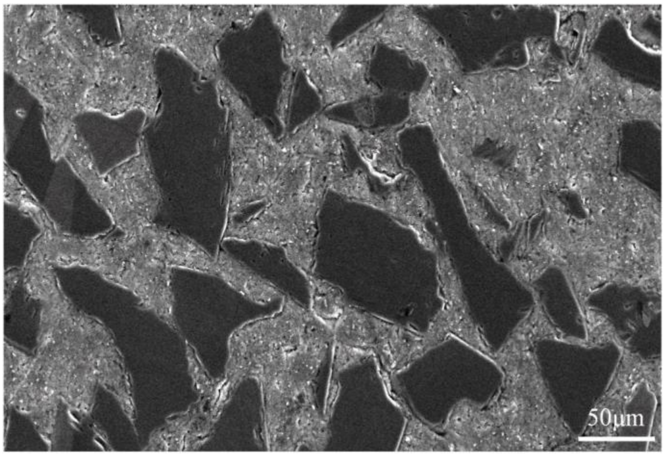

Fig. 4. Microstructure of SiC$_p$/Al composites.

3.1.2. Setup and measurement

The tests were conducted on a 3-axis milling center (Minimill, Haas Inc., USA) and the experimental setup is shown in Fig. 5. A specially customized diamond indenter with a spherical tip radius of 200 μm and an apex angle of 120° was fixed on a rotary ultrasonic machining device which was attached to the spindle of milling center. The distance from the diamond tip to the center of rotation is 10 mm. The rotary ultrasonic machining device has a separate power supply and it can rotate synchronously with the spindle. The working frequency and amplitude were measured using a vibrometer (OFV-5000, Polytec Inc., Germany). The cutting forces (tangential (F_t) and the normal (F_n)) were measured with the assistance of a data acquisition system along with a dynamometer (Type 9257A, Kistler Inc., Switzerland), and the data were recorded with the Dynoware software at a sampling frequency of 5 kHz. The SiC$_p$/Al samples were mounted on a specially customized fixture embedded on a two-dimensional adjustment platform. After tests, the samples were cleaned with an ultrasonic cleaner and the scratch trajectory was studied under a digital microscope (DSX1000, Olympus Inc., Japan) and the morphology of the chips and the scratch tracks were obtained by SEM (JSM7500, JEOL Inc., Japan) to investigate the scratching-induced deformation. The morphology of the subsurface was obtained by SEM (Gemini 300, Zeiss Inc., Germany).

3.2. Experimental procedure

The experiments were divided into two groups (CS & RUVAS), with which CS is scratching without ultrasonic vibration and RUVAS is scratching with ultrasonic vibration. In each group, there were 9 experiments with different set scratch depths and spindle speeds which could be adjusted by the Haas CNC system. The scratch depth was set to 5/10/20 μm. The spindle speed was set to 0/1500/3000/4500/6000 rpm therefore the linear speed of scratching could reach 0/1.57/3.14/

Table 2

Scratch test parameters.

Set scratch depth /μm	Spindle speed /rpm	Ultrasonic frequency /Hz	Ultrasonic amplitude /μm
5,10,20	0,1500,3000, 4500,6000	18000	6

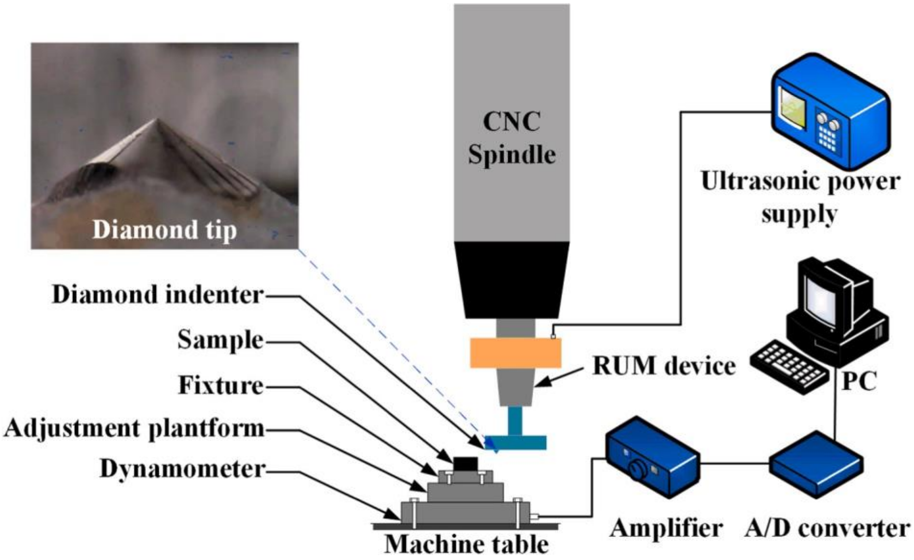

Fig. 5. Experimental setup of RUVAS.

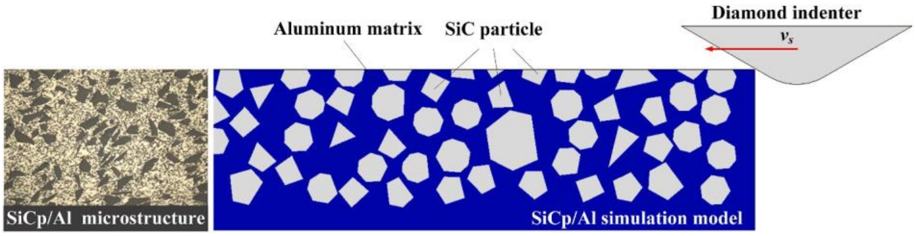

Fig. 6. 2D Finite model of scratching SiC_p/Al.

4.71/6.28 m$\cdot$s^{-1}. When the spindle speed was 0, the feed rate of the sample was set to 0.5 mm$\cdot$min^{-1} to ensure the relative movement of the indenter and the sample. The specific set scratch parameters are listed in Table 2. The samples were accurately positioned using the adjustment platform which has two rotational degrees of freedom to keep the sample flat. The diamond indenter tip was moved to the center of the sample edge before every scratch. A fresh new diamond indenter was used in each group to avoid the influence caused by diamond wear. All experiments were performed at room temperature. The scratch was repeated three times to validate the repeatability of experimental results and the typical experimental results are presented in this paper.

3.3. Finite element modeling

A 2D finite element model was established to investigate the material removal behavior of scratching SiC_p/Al, as shown in Fig. 6. To improve calculation efficiency and accuracy, the model was divided into an equivalent homogeneous plane and particle-matrix composite plane. The dimension of the composite sample had an area of 1.2 mm*0.4 mm. The sample dimensions and volume fraction of particles in the composites model were developed in Abaqus/Explicit using Python scripts. To simplify the calculation, the interface modeling between particles and matrix was neglected and the internal contact between the particles and the matrix is tied together. The CPE4RT unit was selected for model meshing.

The diamond indenter used in the experiment was conical with a top angle of 120°. Therefore, the model of the diamond tool was built as an isosceles triangle with vertex angles of 120°. It was considered a rigid body in the simulation due to its higher hardness compared to the sample material. Also, the scratch depth set in the simulation model was small and the analysis time was short to avoid the deformation and wear of the tool.

The Johnson-cook (J-C) constitutive model and the brittle cracking damage model are adopted to describe the material behavior of matrix and particle respectively. Relevant parameters and models are listed in the appendix.

The finite element model had a meshed of 5 μm size along with an adaptive meshing. The diamond indenter motion was linear with a speed of 1570 mm$\cdot$s^{-1} and the ultrasonic vibration frequency was 18000Hz with an amplitude of 6 μm. The left and bottom edge of the model was fixed to increase the stability of the simulation process. The scratching depths were set at 5 μm, 10 μm, and 20 μm to give an insight into the chip formation and material removal process under intermittent and continuous scratch.

4. Results and discussion

4.1. Simulation results

Fig. 7 illustrates the evolution of the scratch at a depth of 20 μm cut for both conventional and vibratory modes of cutting. For the conventional cutting in Fig. 7a-b, it is observed that the diamond indenter is closer to a cutting tool with a large negative rake. When it touches the SiC_p/Al sample surface, compressive stress is concentrated on the top

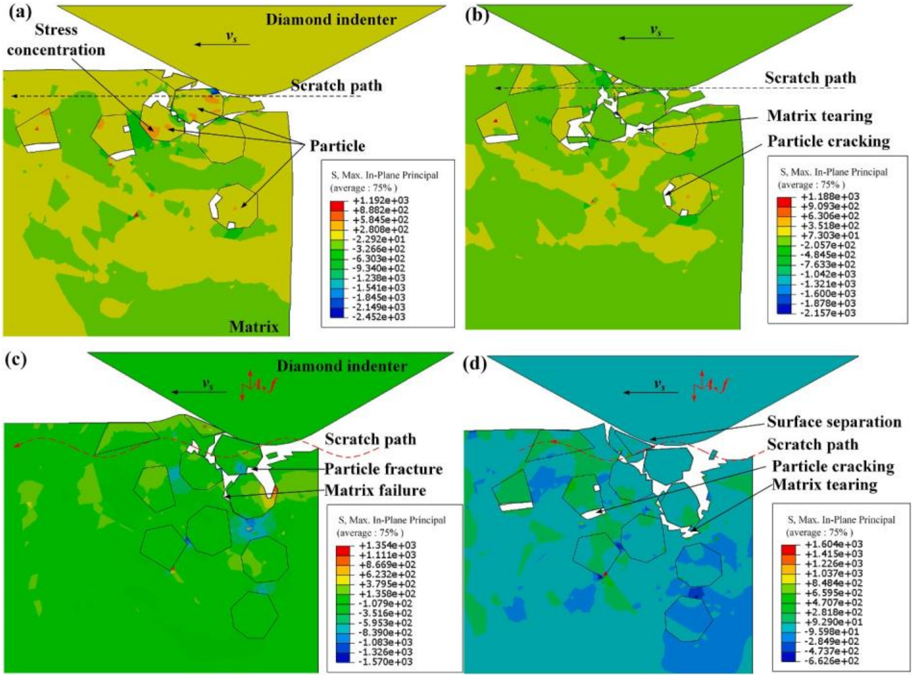

Fig. 7. Principal stress for 20 μm depth: (a–b) conventional, (c–d) with ultrasonic vibration.

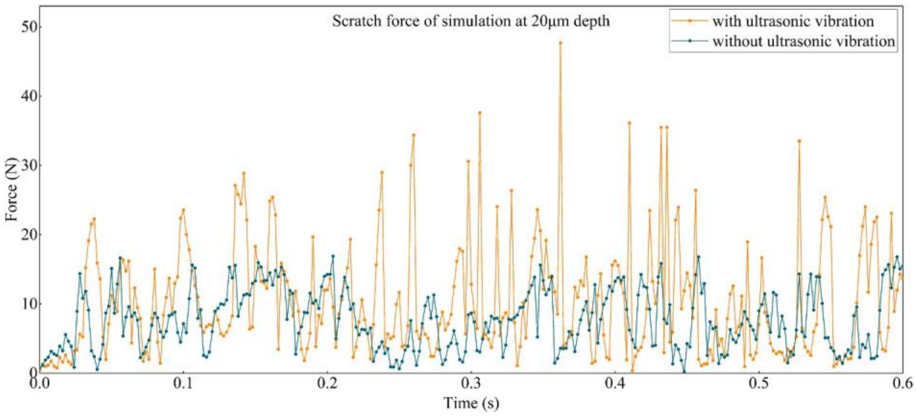

Fig. 8. Scratch force of simulation at depth of 20 μm.

edge of the indenter because of the extrusion. And the tensile stress is distributed around the particles. As the aluminum matrix material is compressed and flows left and down because of its ductility. With the movement of the indenter, the stress transfers to the left and gathers gradually until it reaches the failure strength, which leads to the particle debonding from the matrix or initiation cracking of the particle. Unlike aluminum matrix material, the SiC particle with high modulus deforms slightly. With the initiation and expansion of the crack, a part of the single particle began to fracture and fall off or stagnate on the surface. Because of the continuous contact between the diamond indenter and material, some dislocated particles are pushed by the diamond indenter and scratch the surface again.

Fig. 7c-d. illustrates the simulation results of the scratch process with ultrasonic vibration assisted, which displays a clear difference from the conventional scratch path as the motion of the diamond indenter oscillates. When it moves down the sample surface, the material is not only squeezed by the diamond indenter but also impacted in the vertical direction. The impulse caused by vibration intensifies the stress concentration which accelerates the crack initiation of particles. Because of the high volume fraction of SiC particles, the accumulated deformation of the matrix increases the tensile stress around these dense particles, which results in continuous matrix tearing among the particles. Unlike scratching without ultrasonic vibration, the diamond tool presses into and lifts from the material which makes extracted particles detach from the surface.

The scratch force of the simulation process at 20 μm depth is extracted and shown in Fig. 8. The blue line illustrates the scratch force without ultrasonic vibration. Obviously, the force rises as the diamond indenter contact with the material. Then it increases sharply because the presence of hard SiC particles enhances cutting resistance. And with the detachment of some particles near the surface, the force can also decline to zero. Due to the staggered distribution of particles and matrix, the force change fluctuatingly. The red line shows the scratch force with ultrasonic vibration. Unlike scratch force without ultrasonic vibration, more peaks appear periodically as a result of impact function caused by vibration. When the diamond indenter into the cycle of downward movement, the maximum force with ultrasonic vibration can be more than three times that without ultrasonic vibration. As the movement becomes uplifted, the force sharply goes down.

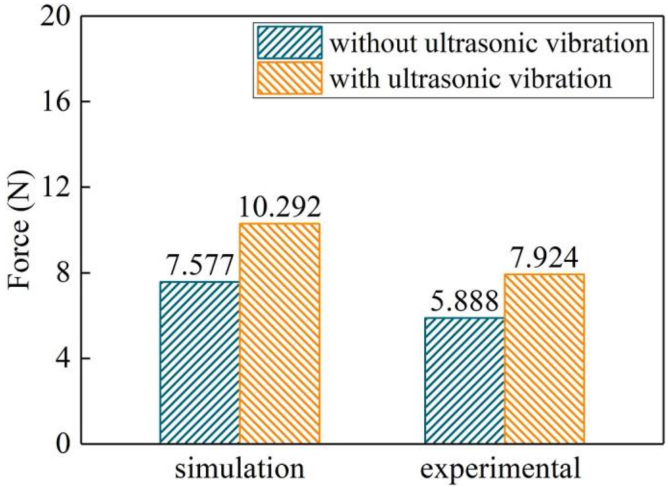

Fig. 9. Average scratch force of simulation and experiment at depth of 20 μm.

Fig. 9 gives the average scratch forces at 20 μm depth of cut both for the simulation and the experiments. Considering the ultrasonic frequency (18 kHz) and the response time of the dynamometer, it is postulated that the dynamometer was not able to capture accurately the cutting forces, and the embedded filter in the data recording system reduced further the magnitude of the measured forces. In addition, to capture the evolution of the cutting in the vibro-impact mode with acceptable accuracy, the data sampling rate should have been at least five times the ultrasonic frequency. On the one hand, both the data acquisition system and the dynamometer had some physical limitations which affected the magnitude of the measured forces. On the other hand, the material physical properties used in the simulation are estimated based on average values found in the literature, therefore the results are an approximation. Consequently, there is a discrepancy of 23% between the simulation and the experimental results. However, there is an increase in ultrasonic cutting force with reference to conventional, which is explained by the fact that ultrasonic actually is more efficient and it removed more material, which led to higher forces. This is supported by the measurement of the actual depth of cut in each scratch test, as illustrated in Fig. 12.

4.2. Scratch trajectory characteristics

According to the kinematic characteristics and scratch force model of RUVAS, the scratch trajectory has a direct relationship with the scratch depth, ultrasonic amplitude, ultrasonic frequency, scratch speed, and material properties. The inequation (14) has shown that with the increase of scratch speed or decrease of frequency, the scratch trajectory tends more into the mode I trajectory, which is shown in Fig. 10. The material is removed intermittently and creates bumps and hollows. When the speed goes down, the scratch trajectory tends more into mode II or III trajectory. There will be an overlap between the pits, and the trajectory will be displayed as a continuous trajectory.

In this research, the change of amplitude and frequency during the scratch process are ignored. As the set scratch depth is 5 μm and the ultrasonic frequency is 18000Hz, the critical velocity for a discontinuous

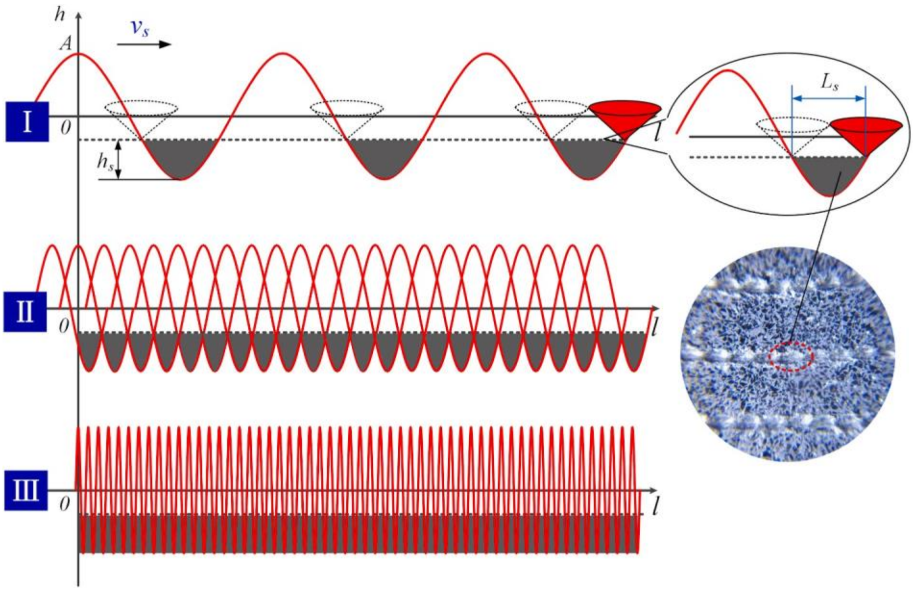

Fig. 10. Various modes of scratch trajectory characteristics.

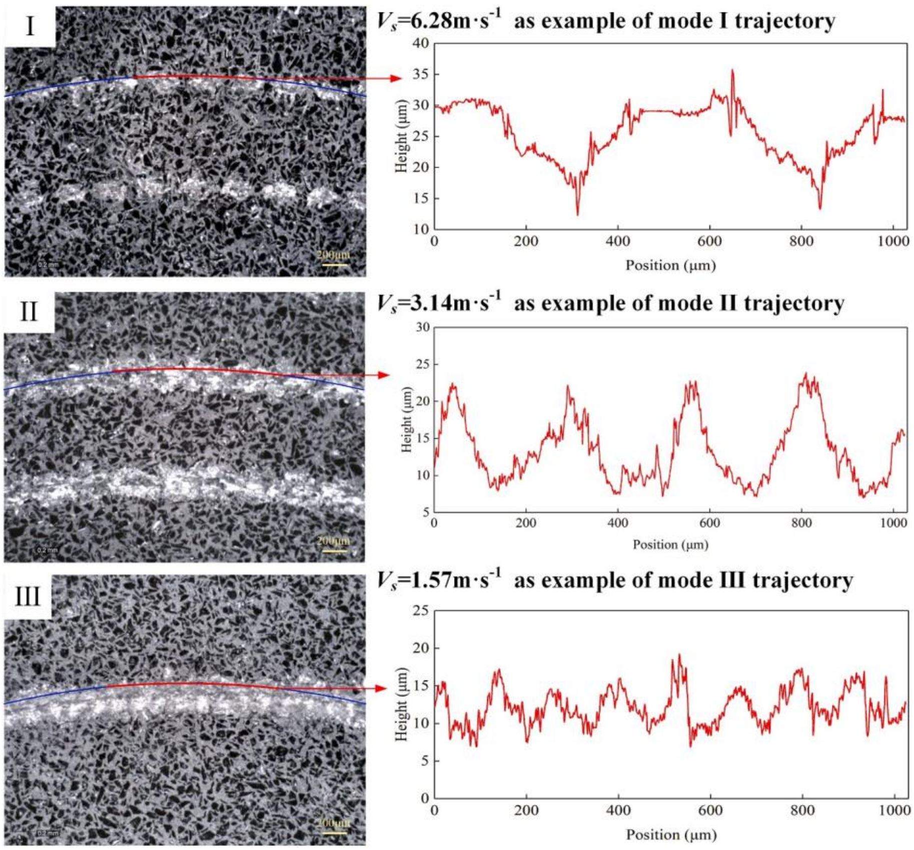

Fig. 11. Scratch trajectory under various speed: (I) 6.28 m s^{-1}, (II) 3.14 m s^{-1}, (III) 1.57 m s^{-1}.

trajectory is calculated as 5252 rpm according to inequation (14). The experiment results showed that the scratch trajectory is continuous when the spindle speed is 1500 rpm or 3000 rpm (1.57 m.s^{-1} or 3.14 m.s^{-1}) as shown in Fig. 11 (II, III). However, when the spindle speed rises to 6000 rpm (6.28 m.s^{-1}), the scratch trajectory turns to be discontinuous as shown in Fig. 11 (I).

For continuous scratch trajectory, the main material removal process contains scratching, plowing, and hammering. The interval between impact zones of each vibration period is small. The cracks extend together and overlap with each other, resulting in continuous removal and peeling of the material. Different from the continuous scratch trajectory, the hammering caused by ultrasonic vibration takes up the main part of the discontinuous scratch trajectory. The intermittent trajectory indicates that the interval between adjacent impact zones is large and the range of crack propagation is small. Thus the material cannot be removed continuously. The number of impacts per scratch length is

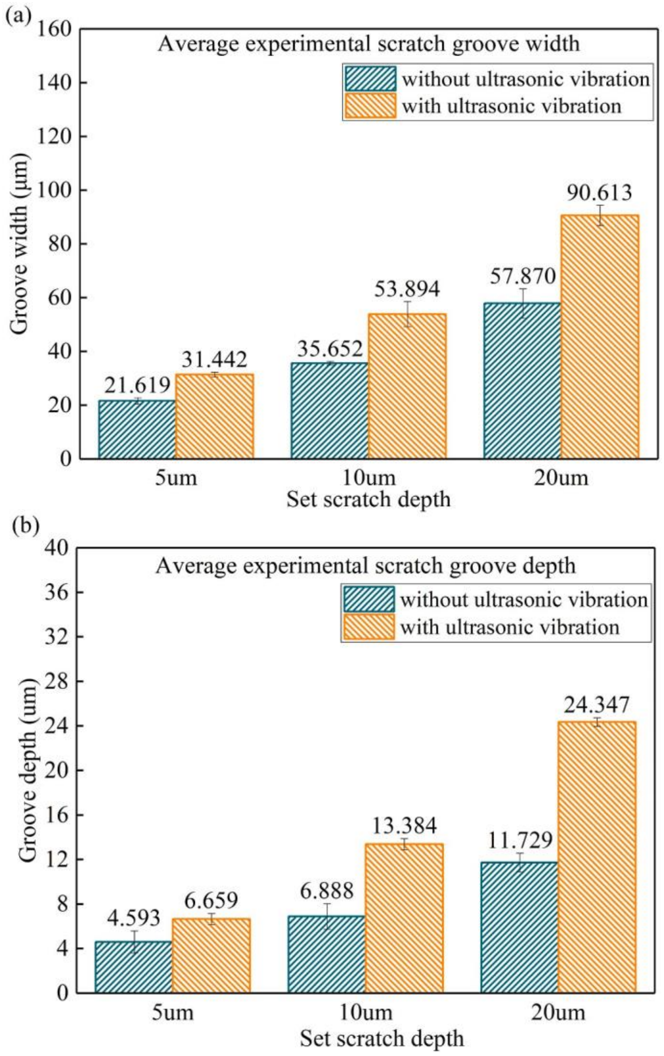

Fig. 12. Experimental scratch groove characteristics: (a) average width, (b) average depth.

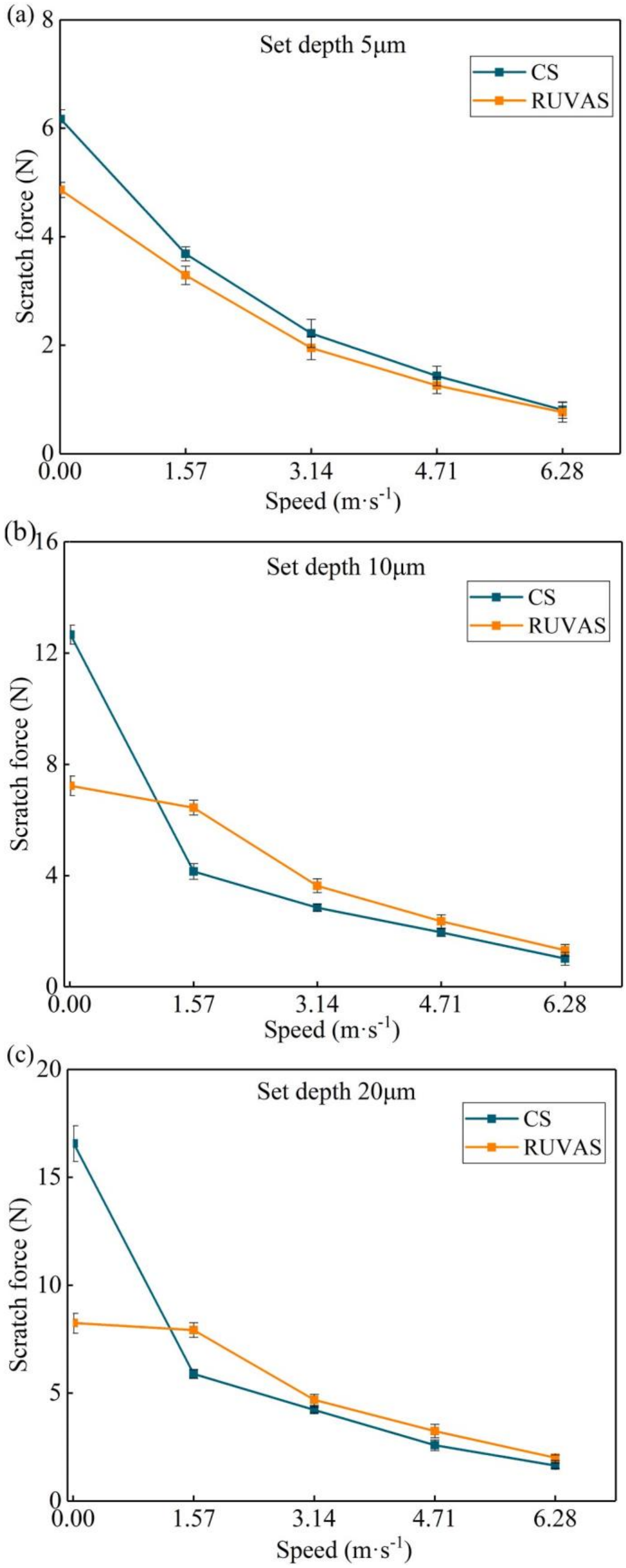

Fig. 13. Scratch force of CS and RUVAS tests at different set scratch depths: (a) 5 μm, (b) 10 μm, (c) 20 μm.

reduced which means that the increase in scratch speed thins the times of ultrasonic impact and forms independent impact pits. This phenomenon gives insight into the matching of ultrasonic vibration parameters and machining parameters. To avoid intermittent trajectory and alleviate the impact of ultrasonic vibration, a high ultrasonic frequency is recommended when the machining speed is high.

4.3. Experimental scratch groove profile

The experimental scratch groove is measured by a laser confocal microscope at the entrance, middle, and exit parts. The result is obtained by calculating the average value of these three points. As shown in Fig. 12a., when the set scratch depth changes from 5 μm to 20 μm, the practical width of the groove stays the same whether with ultrasonic vibration or not. But the practical width of the groove with ultrasonic vibration is about 40% bigger than without ultrasonic vibration. Considering the rebound of material deformation and the fracture wear of diamond tip, normally the practical average scratch depth is smaller than the set scratch depth. But the practical average scratch depth can be larger than the set scratch depth when scratching with ultrasonic vibration. And when with ultrasonic vibration, the practical scratch depth is about 40%–50% larger than the scratch without ultrasonic vibration as shown in Fig. 12b. Because the amplitude of vibration extends the diamond indenter's axial movement which results in a bigger practical scratch depth. It indicates that the vibration effect can accelerate the flow and fracture of material and improve the material removal of $\mathrm{SiC_p}$/Al.

4.4. Scratch force

The scratch force of CS and RUVAS for $\mathrm{SiC_p}$/Al composites are shown in Fig. 13. When the scratch speed is as low as 0.5 $\mathrm{mm \cdot min^{-1}}$, the scratch force with ultrasonic vibration is smaller than without ultrasonic vibration no matter the scratch depth changes from 5 μm to 20 μm, which is consistent with the results in the previous literature [9,10]. And with the increase in scratch depth, the effect of ultrasonic vibration on force reduction is more significant. One reason can be speculated as the contact time between the indenter and the workpiece sample is longer under the action of ultrasonic vibration when the scratch speed is low. The long-term ultrasonic vibration action leads to an ultrasonic softening effect which makes samples easy to cut. When the contact time diminishes as the scratch speed becomes higher, the ultrasonic softening effect is weakened.

As displayed in the chart, both CS and RUVAS forces decrease with the increase of scratch speed when the scratch speed is beyond 1.57 $\mathrm{m \cdot s^{-1}}$. When the set scratch depth is 5 μm, which is similar to the amplitude of ultrasonic vibration, the scratch force of RUVAS is smaller than the force of CS. When the set scratch depth rises to 10 and 20 μm, which is beyond the amplitude of ultrasonic vibration, the scratch force of RUVAS is bigger than the force of CS. However, when the scratch speed reaches 6.28 $\mathrm{m \cdot s^{-1}}$, the scratch force of CS and RUVAS tend to be the same regardless of what scratch depth it is.

According to the scratch force model, it is clear that the scratch force rises when the scratch depth increases, which is coincide with the scratch force data. However, it is noteworthy that the scratch force of RUVAS is smaller than the force of CS when the scratch depth is 5 μm. As the scratch depth is two times or four times larger, the scratch force of RUVAS is much bigger. The reason can be attributed to the kinematic transformation of the ultrasonic vibration-assisted scratch process. When the scratch depth is smaller than the ultrasonic amplitude, the scratch process turns to be intermittent, the practical scratch depth of RUVAS is relevantly smaller than the practical scratch depth of CS, and the scratch force of RUVAS is smaller than that of CS. But when the scratch depth is bigger than the ultrasonic amplitude, the scratch process turns to be continuous without diamond grits' separation from materials, the practical scratch depth of RUVAS relevantly becomes bigger, and the scratch force of RUVAS is larger than that of CS.

Previous research has shown that the ultrasonic vibration-assisted scratch force is smaller than CS at a low speed. It is different from the situation when the scratch speed is high, which means that the scratch speed also has a strong influence on the scratch force. When the set scratch depth is 5 μm, the scratch force of RUVAS is smaller than that of CS at a speed of 1.57 $\mathrm{m \cdot s^{-1}}$ to 4.71 $\mathrm{m \cdot s^{-1}}$. This is because at this stage the intermittent contact of RUVAS alleviates the continuous material removal process of CS. But when the scratch speed rises to 6.28 $\mathrm{m \cdot s^{-1}}$, there is no obvious difference among scratch forces despite ultrasonic vibration assistance, which means the scratch force is insensitive to ultrasonic vibration. Equation (14) has shown that high scratch speed will extend the wavelength λ when the ultrasonic frequency f is fixed. Thus the longer wavelength leads to longer separated pits on the material surface under RUVAS. The material removal process is mainly in the form of impacting the surface. The magnitude of the scratch force is mainly related to the impact depth which is similar to the scratch depth of CS. When set scratch depth is 10 or 20 μm, the scratch force of RUVAS is bigger than that of CS at a speed of 1.57 $\mathrm{m \cdot s^{-1}}$ to 4.71 $\mathrm{m \cdot s^{-1}}$. As scratch turns to continuous contact in this situation, the changing scratch depth added by vibration leads to a bigger force under RUVAS. Because of the constant frequency we used, the RUVAS force shows no significant variation compared with the CS force when scratch speed increases to 6.28 $\mathrm{m \cdot s^{-1}}$.

(a) scratch surface without ultrasonic vibration at depth-5 μm

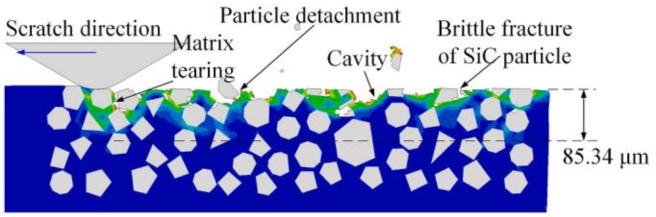

(b) scratch surface with ultrasonic vibration at depth-5 μm

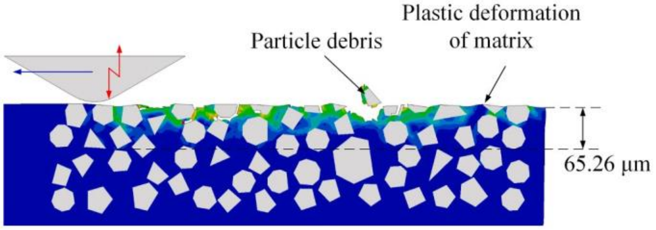

(c) scratch surface without ultrasonic vibration at depth-20 μm

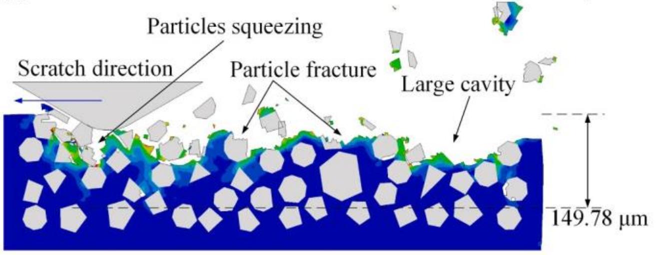

(d) scratch surface with ultrasonic vibration at depth-20 μm

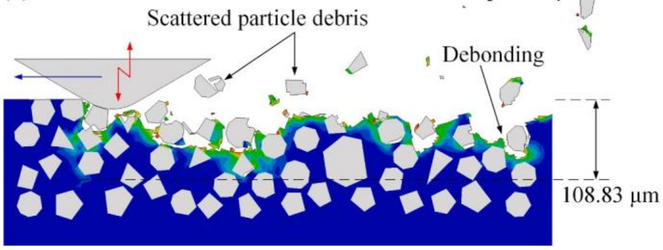

Fig. 14. Scratch surface morphology of simulation:(a) 5 μm depth without ultrasonic vibration, (b) 5 μm depth with ultrasonic vibration, (c) 20 μm depth without ultrasonic vibration, (d) 20 μm depth with ultrasonic vibration.

4.5. Surface morphology

Fig. 14(a-b) shows the simulated scratch surface at a scratch depth of 5 μm. It is clear that the state of particles has a crucial effect on the surface. When the scratching process is not assisted by ultrasonic vibration, the particles are pressed and pushed by a diamond indenter (Fig. 14a). The particles are broken into small pieces or pulled out from the matrix as a whole. Separated small particles leave small pits on the surface. The larger ones wrapped around the matrix and were torn from the surface, creating large cavities. When assisted by ultrasonic vibration, the particles are impacted and pressed by the diamond indenter's intermittent motion (Fig. 14b). The particles sink into the matrix and drive the plastic flow of the matrix. The sliding matrix then causes the particles to debond or detach from the surface.

Fig. 14c-d shows the simulated scratch surface at a scratch depth of 20 μm. When the scratch depth rises, the rake face of the diamond indenter contacts the larger area of the material. In the process of being pressed and pushed by the diamond indenter, the particles will squeeze with each other. In this way, a large number of particles are pulled out and the matrix is torn laterally in a large area, creating large cavities

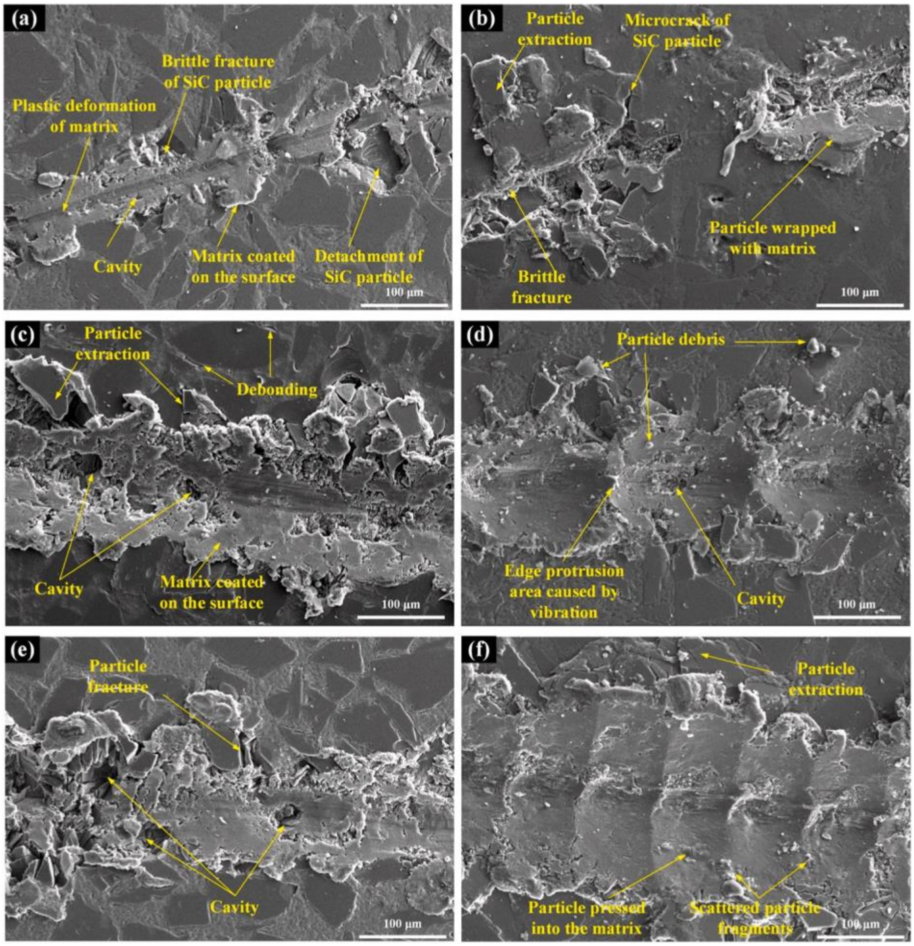

Fig. 15. Scratch morphology of CS and RUVS at set depth: (a–b) 5 μm, (c–d) 10 μm, (e–f) 20 μm.

(Fig. 14c). However, with ultrasonic vibration, the material is subjected to continuous vibration and impact, causing break down of a large number of particles, and the matrix is torn longitudinally. This results in small, scattered particle debris and edge breakage, which is shown in Fig. 14d.

Fig. 15 exhibits the microstructure of the experimental scratch surfaces at different scratch depths without and with the assistance of ultrasonic vibration. Obviously, the main deformation form of the SiC_p/Al composites in the scratch process can be divided into plastic deformation of aluminum alloy matrix and brittle fracture of SiC particles. When scratch depth rises from 5 μm to 20 μm without ultrasonic vibration, there are typical scratched surface features such as cavities, particle extraction, particle debonding, and matrix coated on the surface (Fig. 15a,c,15e). The scratch trajectory is the mode I trajectory which is discontinuous at this depth due to the vibration separation effect (Fig. 15b). It is different that brittle fracture takes up the main form of material removal mode. The surface demonstrates more obvious particle fracture and deeper crack propagation. There is no coating of aluminum alloy matrix on both sides of the scratch trajectory. Fig. 15d shows the morphology of mode II trajectory which is edge overlapped for every pit removed per vibration cycle. The bottom surface of these pits is relatively flat. But there are joint marks and cracks on the surface at the

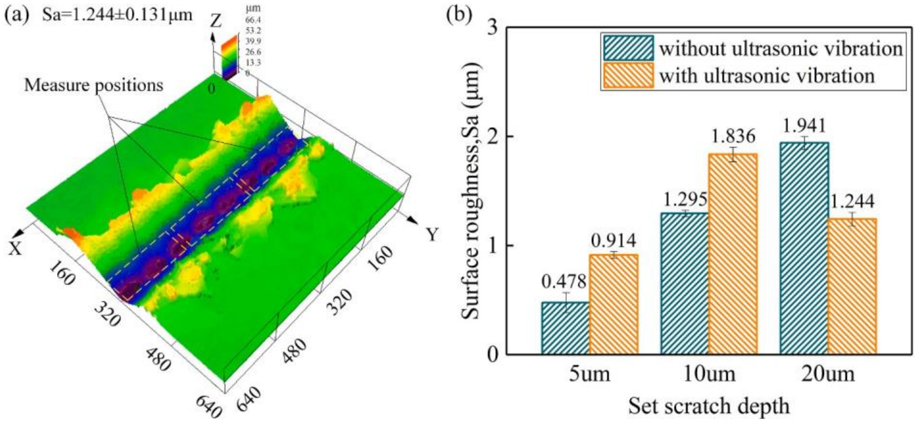

Fig. 16. Surface roughness of CS and RUVS: (a) measurement, (b) surface roughness, Sa.

junction of the edges of the pits. Small particle debris can be observed. Some of them are scattered in the pit, while others fly out to both sides of the scratch groove. Fig. 15f shows the morphology of mode III trajectory which is more area overlapped for every pit removed per vibration cycle. Due to the repeated vibration impact, the width of the scratch groove becomes significantly larger. Although the particles are hammered into smaller debris in this mode, they are pressed into the matrix under the action of repeated impact. And the aluminum alloy is repeatedly coated on the surface, which leads to better surface integrity.

The 3D surface roughness Sa of the scratch surface is measured to evaluate the surface integrity (Fig. 16a) and the results are shown in Fig. 16b. The 3D surface roughness agrees well with the surface morphology results. And the scratch surface quality is mainly related to the particle state, coated matrix, and, overlapping area caused by ultrasonic vibration. An increase in the set scratch depth leads to a bigger 3D surface roughness of the scratch surface obtained without ultrasonic vibration. This is because more particles are broken or pulled out from the matrix, leaving small particle debris and cavities on the surface. Some particle debris can scratch the surface again leading to worse surface integrity. The 3D surface roughness of the scratch surface with the presence of ultrasonic vibration is bigger than that without when the scratch depth is 5 μm and 10 μm. And the surface roughness with ultrasonic vibration is smaller than that without ultrasonic vibration when the scratch depth is 20 μm. This is because the discontinuous scratch trajectory has a significant influence on surface integrity. When the scratch depth rises to 20um and the scratch trajectory is in mode III, the edge protrusions caused by vibration are erased. This is because of the overlapping superposition of vibration trajectories. The surface cavities and small particle debris are coated by the flowing aluminum alloy matrix on the surface.

4.6. Subsurface morphology

Fig. 15 shows the subsurface morphology of the scratched surface

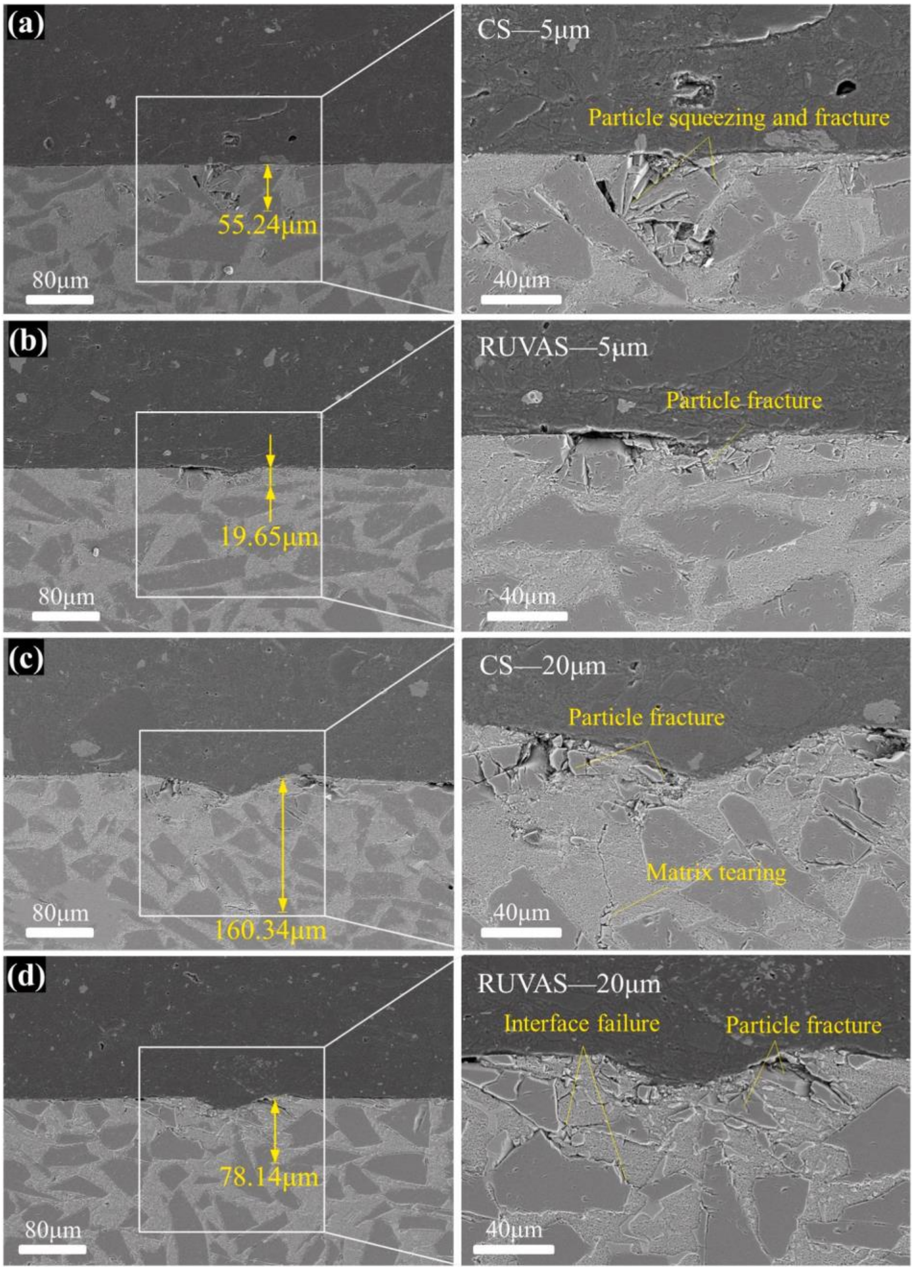

Fig. 17. Subsurface morphology of CS and RUVAS at set depth: (a,b) 5 μm, (c,d) 20 μm.

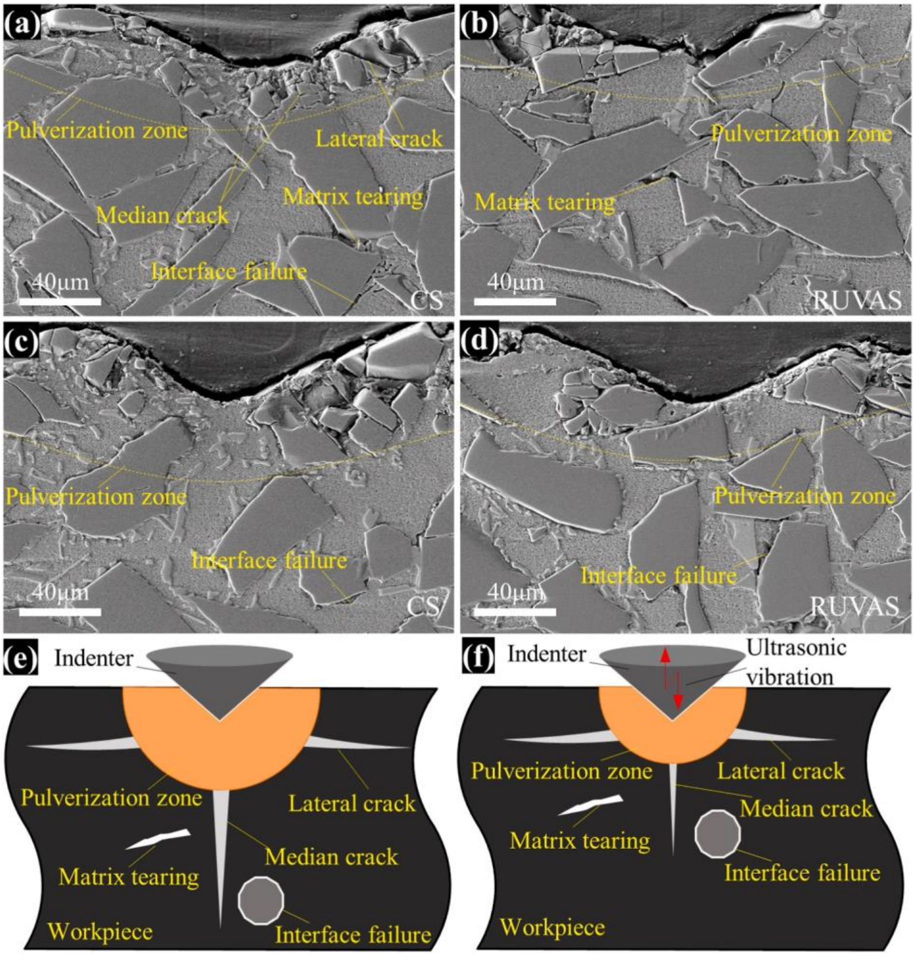

Fig. 18. Subsurface damage of CS and RUVAS: (a,b) practical scratch depth of 30 μm, (c,d) practical scratch depth of 40 μm, (e,f) formation mechanism.

under simulation. Due to the interaction between the diamond indenter and the composites, internal stress has undergone transmission and cumulation, leading to the initiation and propagation of cracks, fracture of particles, and tearing and debonding of the matrix. Furthermore, with the increase of cutting depth, the depth of the subsurface damage layer rises. However, when compared to CS, the depth of the subsurface damage layer under RUVAS is smaller. This may be related to the contact separation between the tool and the material during the simulation process, which reduces the accumulation of stress.

The cross-section of the test samples along the scratch direction is polished and then observed. The morphology of the subsurface of the scratching specimen is shown in Fig. 17. Regardless of scratch technique, the matrix tearing, interface debonding, and particle fracture are the main forms of subsurface damage. When the scratch depth is 5 μm, due to the dense particle distribution and the lack of buffer effect, obvious particle squeezing and fracture occurred under CS. Noticeably, the depth of the damaged layer can reach up to 55.24 μm (Fig. 17a). When comparing RUVAS to CS, particle fracture also occurs in the area with dense particle distribution, but the depth of the damaged layer is only 35.59% of CS (Fig. 17b). When the scratch depth goes further to 20 μm, matrix tearing was observed, and the depth of the damage layer can reach up to 160.34 μm (Fig. 17c). However, the damage layer depth of RUVAS is only 48.73% of CS (Fig. 17d). Similar with the simulation results, there are different degrees and ranges of damage on the subsurface of SiC_p/Al composites in the scratching test. Compared with CS, the depth of the damage layer under RUVAS is smaller, which not only validates the simulation results but also reflects the fact that ultrasonic vibration can effectively reduce the subsurface damage of SiC_p/Al composites during scratching.

To better understand the subsurface damage in the scratching process of SiC_p/Al composites, Fig. 18 shows the subsurface morphology under practical scratching depth (30 μm,40 μm). It can be concluded that the typical subsurface damage of SiC_p/Al composites includes particle cracking and fracture, matrix tearing, and interface failure. Whether CS or RUVAS, there is a pulverization zone [31,32] filled with broken particles at the subsurface of SiC_p/Al composites. Different from CS, the pulverization zone under RUVAS is smaller (Fig. 18e&f). This may be explained by that when the diamond indenter presses against the surface of the composites under CS, compressive stress is generated in the matrix and particles. When there is no vibration, this stress will continue to accumulate, transfer, and gather inside the material, and the internal defects of the composites can be triggered under load, thus triggering the nucleation, propagation, and interdigitation of microcracks, as well as more fragmentation in the subsurface layer. While under RUVAS, the indenter vibrates up and down at a high frequency along the material surface. When the indenter moves away from the material surface, a certain stress relaxation effect is produced. The stress does not accumulate continuously, which reduces the transmission and concentration of internal stress inside the composites and only causes damage near the surface area (Fig. 18b&d).

As a typically hard and brittle material, there are lateral and median cracks in the high-volume fraction SiC_p/Al composites under the extrusion of diamond indenter (Fig. 18a). Compared with CS, fewer median cracks are observed under RUVAS, and the depth of matrix tearing and interface failure are smaller(Fig. 18e&f). This can be explained by the reason that the direction of scratching is different from the propagation direction of the median crack. Under ultrasonic scratching, the instantaneous scratching speed is much bigger than that of CS. The propagation time of the median crack is less before the indenter passes, resulting in a smaller depth of subsurface damage layer under ultrasonic scratching. This phenomenon is also found in ultrasonic vibration machining of brittle materials such as K9 glass and mono-crystalline silicon [33,34].

5. Conclusions

We addressed the rotary ultrasonic vibration assisted scratch (RUVAS) test and conventional scratch (CS) test for high volume fraction SiC_p/Al at various speeds theoretically and experimentally in this study. The following conclusions could be drawn:

(1) The scratch simulation demonstrated that the material removal mechanism of SiC_p/Al is mainly composed of plastic deformation of aluminum matrix and brittle fracture of SiC particles. In ultrasonic scratching, the hard SiC particles are more likely to be ruptured under a high strain rate of impact function and facilely squeezed into the aluminum alloy matrix due to the plastic flow caused by the acoustic softening effect. This process can inhibit crack initiation and propagation while healing the defects such as craters, chipping, and cracking, giving better surface integrity. With ultrasonic vibration assistance, the average scratch force is larger and fluctuates with the motion of the vibration. The subsurface stress is obviously reduced, and the stress-affected zone becomes smaller than without ultrasonic vibration assistance.

(2) The scratch trajectory indicated that the trajectory mode is affected by scratch speed, scratch depth, ultrasonic amplitude, and frequency. Under intermittent trajectory mode, the impact effect of ultrasonic vibration takes up the main part of the material removal mode. To keep the trajectory continuous, the ultrasonic parameters, crack propagation characteristics of materials, and cutting parameters must be considered simultaneously when machining SiC_p/Al.

(3) The experimental scratch force of RUVAS and CS showed that the scratch force is smaller with ultrasonic vibration assisted when the scratch speed was low at intermittent scratch mode. The scratch force is higher with ultrasonic vibration assistance when the scratch is in continuous mode as the scratch groove profile proves that a larger scratch groove width and depth are obtained by ultrasonic vibration. Unlike the low-speed ultrasonic vibration-assisted scratch test of SiC_p/Al, the scratch force only demonstrated a minor difference between RUVAS and CS when the scratch speed is 6.28 m·s^{-1}. The matching relation between ultrasonic parameters and scratching parameters was proposed considering the kinematics and material behavior to guarantee the effectiveness of ultrasonic vibration, guiding the vibration-assisted processing of advanced composites.

(4) The morphology of SiC_p/Al samples suggested that the state of SiC particles had a significant effect on surface integrity. The intermittent scratch mode will lead to a surface with independent pulsed pits which should be avoided in SiC_p/Al machining. The superposition of vibration trajectories can make up for the holes where the particles break and detach, and cover the particle debris and cavities on the surface with the matrix, leading to better surface integrity.

(5) The subsurface morphology of SiC_p/Al samples illustrated that subsurface damage is inevitable in both CS and RUVAS. The cracking and fracture of particles, matrix tearing, and interface debonding are the main forms of subsurface damage. Compared with CS, the depth and scope of subsurface damage under RUVAS are smaller. This may be explained by the stress relaxation effect caused by ultrasonic vibration and 'the skin effect' under RUVAS.

Declaration of competing interest

The authors declare that they have no known competing financial interests or personal relationships that could have appeared to influence the work reported in this paper.

Acknowledgment

Special thanks to Blair for the revision of the language and YU Qun for the surface observation. This work was supported by the National Natural Science Foundation of China [grant number U1737201].

Appendix

A. Material behavior of the simulation

Johnson-cook (J-C) constitutive model is widely used to describe the elastoplastic behavior of ductile materials [35]. To characterize the aluminum matrix material behavior, a modified J-C constitutive criterion [20] was adopted.

$$\sigma = (A + B\varepsilon^n)\left[1 + C\ln\left(\frac{\dot{\varepsilon}}{\dot{\varepsilon}_0}\right)\right]\left[1 - \left(\frac{T - T_{room}}{T_{melt} - T_{room}}\right)^m\right] \tag{A.1}$$

where **σ** is the equivalent stress, ***A*** is the yield stress, ***B*** is the hardening modulus, ***C*** (=0.01) is the coefficient of strain rate sensitivity, ***m*** is the coefficient of thermal softening, ***n**** is the coefficient of hardening, $\dot{\varepsilon}$ and $\boldsymbol{\varepsilon^n}$ are the plastic strain and strain rate; $\dot{\varepsilon}_0$ (=1.47*$10^5 s^{-1}$) is the reference plastic strain rate, ***T*** is the temperature of the material, $\boldsymbol{T_{melt}}$ is the melting temperature and $\boldsymbol{T_{room}}$ is the room temperature.

The Johnson-Cook damage model was used to describe the aluminum matrix failure behavior.

$$D = \sum \frac{\Delta\varepsilon^{pl}}{\varepsilon_f^{pl}} \tag{A.2}$$

where ***D*** is the damage variable, and when its value goes to 1, the failure happens. $\boldsymbol{\Delta\varepsilon_f^{pl}}$ is the increment of equivalent plastic strain, $\boldsymbol{\varepsilon_f^{pl}}$ is the equivalent plastic strain when material failure, which can be expressed by

$$\varepsilon_f^{pl} = [D_1 + D_2\exp(D_3\sigma^*)]\left[1 + D_4\ln\left(\frac{\dot{\varepsilon}}{\dot{\varepsilon}_0}\right)\right]\left[1 + D_5\left(\frac{T - T_{room}}{T_{melt} - T_{room}}\right)\right] \tag{A.3}$$

where $\boldsymbol{D_1}$, $\boldsymbol{D_2}$...$\boldsymbol{D_5}$ are the damage variable of materials, and $\boldsymbol{\sigma^*}$ is the stress triaxiality.

The above parameters about the aluminum matrix used in this simulation are listed in Table A.1.

Table A.1
J-C model parameters of the aluminum matrix.

A/MPa	255
B/MPa	361
m	5.5
n	0.18
T_{melt}/K	652
T_{room}/K	295
D_1	0.004
D_2	0.237
D_3	2.775
D_4	0
D_5	0.16

The SiC particles undergo a linear elastic deformation when subjected to an external load. The criterion for the initiation of fracture of particles is considered as the maximum principal tensile stress $\boldsymbol{\sigma_t}$, which goes beyond the tensile strength of SiC particles. The Rankine criterion was adopted to describe the particles fracture behavior during scratching, which can be described by

$$\mathrm{Max}(\sigma_1, \sigma_2, \sigma_3) = \sigma_t \tag{A.4}$$

After the initiation, the crack starts to extend and propagate and with the energy-based cracking criteria proposed by Ref. [36], there is a linear relationship between material strength and crack scale. When the displacement reaches the crack normal displacement $\boldsymbol{U_n}$, the particle fails, which can be expressed by

$$U_n = \frac{2G_f^{\mathrm{I}}}{\sigma_t} \tag{A.5}$$

Where *GI f* is the fracture energy of Mode I crack, expressed as

$$G_f^{\mathrm{I}} = \frac{K_{IC}^2}{E'} \tag{A.6}$$

where *K2 IC* is the fracture toughness and E' is the equivalent of Young's modulus. The shear modulus was defined as a function of crack opening strain to describe the effect of shear stress on crack growth, consequently, the shear modulus G_c after crack initiation was defined as

$$G_c = \rho\left(e_{nm}^{ck}\right)G \tag{A.7}$$

where *G* is the shear modulus, ρ(*eck nm*) is the shear retention factor which can be expressed by

$$\rho\left(e_{nm}^{ck}\right) = \left(1 - \frac{e_{nm}^{ck}}{e_{\max}^{ck}}\right)^{P} \tag{A.8}$$

where *eck nm* is the strain of crack opening, *eck max* and *P* are material parameters of SiC particle. Therefore, in the simulation, the parameters given in Table A.2 were used.

Table A.2
Brittle cracking damage model parameters of SiC.

K_{IC}/MPa · m$^{0.5}$	σ_t/MPa	E'/GPa	eck nm	P
4.5	1000	488	0.001	1

References

[1] N. Chawla, K.K. Chawla, Metal Matrix Composites, Springer, New York, 2013, https://doi.org/10.1002/0471238961.1305200103080123.a01. New York.

[2] N. Natarajan, V. Krishnaraj, J.P. Davim, Metal Matrix Composites, Springer International Publishing, Cham, 2015, https://doi.org/10.1007/978-3-319-02985-6.

[3] L. Zhang, Z. Wu, C. Wu, Q. Wu, On the numerical modeling of composite machining, Composites, Part B. 241 (2022), 110023, https://doi.org/10.1016/j.compositesb.2022.110023.

[4] P. Feng, Research status and future prospects of rotary ultrasonic machining of hard and brittle materials, JME (J. Med. Ethics) 53 (2017) 3, https://doi.org/10.3901/JME.2017.19.003.

[5] A. Pramanik, Developments in the non-traditional machining of particle reinforced metal matrix composites, Int. J. Mach. Tool Manufact. 86 (2014) 44–61, https://doi.org/10.1016/j.ijmachtools.2014.07.003.

[6] Z. Yang, L. Zhu, G. Zhang, C. Ni, B. Lin, Review of ultrasonic vibration-assisted machining in advanced materials, Int. J. Mach. Tool Manufact. 156 (2020), 103594, https://doi.org/10.1016/j.ijmachtools.2020.103594.

[7] W. Yu, J. Chen, W. Ming, Q. An, M. Chen, Experimental and FEM study of cutting mechanism and damage behavior of ceramic particles in orthogonal cutting SiCp/

Al composites, Ceram. Int. 47 (2021) 7183–7194, https://doi.org/10.1016/j.ceramint.2020.11.072.

[8] G. Liu, D. Xiang, P. Peng, Y. Li, Z. Yuan, Z. Zhang, G. Gao, B. Zhao, Establishment of scratching force model for micro-removal of SiCp/Al composites by ultrasonic vibration, J. Mater. Process. Technol. 307 (2022), 117677, https://doi.org/10.1016/j.jmatprotec.2022.117677.

[9] P. Feng, G. Liang, J. Zhang, Ultrasonic vibration-assisted scratch characteristics of silicon carbide-reinforced aluminum matrix composites, Ceram. Int. 40 (2014) 10817–10823, https://doi.org/10.1016/j.ceramint.2014.03.073.

[10] W. Zheng, Y. Wang, M. Zhou, Q. Wang, L. Ling, Material deformation and removal mechanism of SiCp/Al composites in ultrasonic vibration assisted scratch test, Ceram. Int. 44 (2018) 15133–15144, https://doi.org/10.1016/j.ceramint.2018.05.150.

[11] Z. Li, S. Yuan, J. Ma, J. Shen, A.D.L. Batako, Study on the surface formation mechanism in scratching test with different ultrasonic vibration forms, J. Mater. Process. Technol. 294 (2021), 117108, https://doi.org/10.1016/j.jmatprotec.2021.117108.

[12] F. Zheng, R. Kang, Z. Dong, J. Guo, J. Liu, J. Zhang, A theoretical and experimental investigation on ultrasonic assisted grinding from the single-grain aspect, Int. J. Mech. Sci. 148 (2018) 667–675, https://doi.org/10.1016/j.ijmecsci.2018.09.026.

[13] S. Huang, L. Guo, H. He, L. Xu, Study on characteristics of SiCp/Al composites during high-speed milling with different particle size of PCD tools, Int. J. Adv. Manuf. Technol. 95 (2018) 2269–2279, https://doi.org/10.1007/s00170-017-1350-6.

[14] C. Liu, W. Ding, T. Yu, C. Yang, Materials removal mechanism in high-speed grinding of particulate reinforced titanium matrix composites, Precis. Eng. 51 (2018) 68–77, https://doi.org/10.1016/j.precisioneng.2017.07.012.

[15] J. Wang, J. Zhang, P. Feng, P. Guo, Damage formation and suppression in rotary ultrasonic machining of hard and brittle materials: a critical review, Ceram. Int. 44 (2018) 1227–1239, https://doi.org/10.1016/j.ceramint.2017.10.050.

[16] W. Bai, A. Roy, R. Sun, V.V. Silberschmidt, Enhanced machinability of SiC-reinforced metal-matrix composite with hybrid turning, J. Mater. Process. Technol. 268 (2019) 149–161, https://doi.org/10.1016/j.jmatprotec.2019.01.017.

[17] Z. Dong, F. Zheng, X. Zhu, R. Kang, B. Zhang, Z. Liu, Characterization of material removal in ultrasonically assisted grinding of SiCp/Al with high volume fraction, Int. J. Adv. Manuf. Technol. 93 (2017) 2827–2839, https://doi.org/10.1007/s00170-017-0676-4.

[18] M. Zhou, M. Wang, G. Dong, Experimental investigation on rotary ultrasonic face grinding of SiCp/Al composites, Mater. Manuf. Process. 31 (2016) 673–678, https://doi.org/10.1080/10426914.2015.1025962.

[19] T.H. KOSEL, Review of Scratch Test Studies of Abrasion Mechanisms, Micro Indentation Techniques in Materials Science and Engineering, ASTM Publication, 1986, p. 889, https://doi.org/10.1520/STP32961S.

[20] G. Yin, Y. Gong, Y. Li, J. Song, Y. Zhou, Modeling and evaluation in grinding of SiCp/Al composites with single diamond grain, Int. J. Mech. Sci. 163 (2019), 105137, https://doi.org/10.1016/j.ijmecsci.2019.105137.

[21] Q. Wu, W. Xu, L. Zhang, Machining of particulate-reinforced metal matrix composites: an investigation into the chip formation and subsurface damage, J. Mater. Process. Technol. 274 (2019), 116315, https://doi.org/10.1016/j.jmatprotec.2019.116315.

[22] Y. Li, X. Ge, H. Wang, Y. Hu, F. Ning, W. Cong, C. Ren, Study of material removal mechanisms in grinding of C/SiC composites via single-abrasive scratch tests, Ceram. Int. 45 (2019) 4729–4738, https://doi.org/10.1016/j.ceramint.2018.11.165.

[23] Q. Liu, G. Huang, C. Cui, Z. Tong, X. Xu, Investigation of grinding mechanism of a 2D Cf/C–SiC composite by single-grain scratching, Ceram. Int. 45 (2019) 13422–13430, https://doi.org/10.1016/j.ceramint.2019.04.041.

[24] F. Zhao, B. Lin, Y. He, T. Sui, Cross-point effect of high-speed cross scratch on hard brittle materials, Ceram. Int. 47 (2021) 9317–9324, https://doi.org/10.1016/j.ceramint.2020.12.059.

[25] J. Feng, X. Huang, S. Yang, J. Qing, P. Tang, Z. Wan, Speed effect on the material behavior in high-speed scratching of BK7 glass, Ceram. Int. 47 (2021), 19978, https://doi.org/10.1016/j.ceramint.2021.04.008. –19988.

[26] B. Meng, D. Yuan, S. Xu, Study on strain rate and heat effect on the removal mechanism of SiC during nano-scratching process by molecular dynamics simulation, Int. J. Mech. Sci. 151 (2019) 724–732, https://doi.org/10.1016/j.ijmecsci.2018.12.022.

[27] J. Cao, Y. Wu, D. Lu, M. Fujimoto, M. Nomura, Material removal behavior in ultrasonic-assisted scratching of SiC ceramics with a single diamond tool, Int. J. Mach. Tool Manufact. 79 (2014) 49–61, https://doi.org/10.1016/j.ijmecsci.2018.12.022.

[28] H. Wang, F. Ning, Y. Li, Y. Hu, W. Cong, Scratching-induced surface characteristics and material removal mechanisms in rotary ultrasonic surface machining of CFRP, Ultrasonics 97 (2019) 19–28, https://doi.org/10.1016/j.ultras.2019.04.004.

[29] D.B. Marshall, B.R. Lawn, A.G. Evans, Elastic/plastic indentation damage in ceramics: the lateral crack system, J. Am. Ceram. Soc. 65 (1982) 561–566, https://doi.org/10.1111/j.1151-2916.1982.tb10782.x.

[30] H.H.K. Xu, S. Jahanmir, L.K. Ives, Mechanisms of material removal in abrasive machining of ceramics, Interceram: International Ceramic Review 47 (1998) 380–386.

[31] B. Zhang, J. Yin, The 'skin effect' of subsurface damage distribution in materials subjected to high-speed machining, Int. J. Extrem. Manuf. 1 (2019), 012007, https://doi.org/10.1088/2631-7990/ab103b.

[32] X. Yang, B. Zhang, Material embrittlement in high strain-rate loading, Int. J. Extrem. Manuf. 1 (2019), 022003, https://doi.org/10.1088/2631-7990/ab263f.

[33] J. Wang, C. Zhang, P. Feng, J. Zhang, A model for prediction of subsurface damage in rotary ultrasonic face milling of optical K9 glass, Int. J. Adv. Manuf. Technol. 83 (2016) 347–355, https://doi.org/10.1007/s00170-015-7567-3.

[34] Y. Wang, B. Zhao, S. Huang, Z. Qian, Study on the subsurface damage depth of monocrystalline silicon in ultrasonic vibration assisted diamond wire sawing, Eng. Fract. Mech. 258 (2021), 108077, https://doi.org/10.1016/j.engfracmech.2021.108077.

[35] G.R. Johnson, W.H. Cook, Fracture characteristics of three metals subjected to various strains, strain rates, temperatures and pressures, Eng. Fract. Mech. 21 (1985) 31–48, https://doi.org/10.1016/0013-7944(85)90052-9.

[36] A. Hillerborg, M. Modéer, P.-E. Petersson, Analysis of crack formation and crack growth in concrete by means of fracture mechanics and finite elements, Cement Concr. Res. 6 (1976) 773–781, https://doi.org/10.1016/0008-8846(76)90007-7.